nature communications

Article

https://doi.org/10.1038/s41467-025-63901-5

Programmable afterglow tuning in monodisperse SiO_2 microparticles through spatially confined emitter doping

Received: 23 December 2024

Accepted: 29 August 2025

Xue Chen[1], **Zhenyu Gong**[2], **Chenxi Peng**[1], **Tian Bai**[3], **Zhongbin Wu**[1], **Weidong Xu**[1], **Xiaowang Liu**[1] ✉ & **Wei Huang**[1,4,5] ✉

Developing monodisperse microparticles with tailored afterglow properties is crucial for optoelectronic applications, achieving afterglow tuning in uniform microsized platforms remains a significant challenge. Here, we present programmable afterglow tuning in monodisperse SiO_2 MPs through spatially confined emitter doping, creating core@shell@shell SiO_2 MPs. By repeatedly performing pseudomorphic transformation, we achieve spatially confined doping of 4-phenylpyridine, 4,4′-bipyridine, and 1,8-naphthalimide into different layers. This method enables afterglow color output from blue to cyan and orange by shifting main excitation from 250 to 350 nm. It also allows tuning of afterglow lifetime and quantum yields of the dopants by gradually enhancing dopant-matrix interactions through repeating hydrothermal reactions. Additionally, altering the doping positions further controls the optical properties due to a combined screen effect by the outer SiO_2 matrix and dopants. Our approach enables the creation of a versatile library of optically active SiO_2 MPs with finely tuned properties, paving the way for advanced photonic crystal platforms for optical encoding and spontaneous emission regulation.

The development of afterglow materials opens up numerous possibilities across diverse sectors, encompassing sustainable lighting[1–3], response systems[4–7], security enhancements[8–10], medical diagnostics[11,12], and nondestructive testing applications[13,14]. Traditional inorganic afterglow phosphors have conventionally been synthesized using high-temperature methods aimed at inducing defect formation for efficient excitation energy trapping. However, this method often leads to limited control over the morphology of the afterglow materials, which in turn restricts their potential applications. In contrast, organic afterglow materials have emerged as compelling alternatives to their inorganic counterparts in recent years, benefiting from more manageable synthetic conditions[15–17]. In organic materials, the afterglow mechanism mainly arises from the stabilization of triplet states of organic emitters through diverse interactions with host matrices, including covalent bonding, hydrogen bonding, physical fixation, or their combinations[18–23]. This straightforward synthetic strategy enables organic afterglow materials to offer significant flexibility in afterglow color tuning by selecting appropriate organic emitters, albeit with an increased vulnerability to

---

[1]State Key Laboratory of Flexible Electronics (LoFE), Frontiers Science Centre for Flexible Electronics (FSCFE), MIIT Key Laboratory of Flexible Electronics (KLoFE), Shaanxi Key Laboratory of Flexible Electronics, Xi'an Key Laboratory of Flexible Electronics, Xi'an Key Laboratory of Biomedical Materials & Engineering, Xi'an Institute of Flexible Electronics, Institute of Flexible Electronics (IFE), Northwestern Polytechnical University, Xi'an, Shaanxi, China. [2]School of Automation, Northwestern Polytechnical University, Xi'an, Shaanxi, China. [3]Shaanxi Key Laboratory of Biomedical Metallic Materials, Northwest Institute for Non-Ferrous Metal Research, Xi'an, China. [4]State Key Laboratory of Flexible Electronics (LoFE), Nanjing University of Posts & Telecommunications, Nanjing, China. [5]Key Laboratory of Flexible Electronics (KLOFE), Institute of Advanced Materials (IAM), Nanjing Tech University (Nanjing Tech), Nanjing, China. ✉e-mail: iamxwliu@nwpu.edu.cn; vc@nwpu.edu.cn

quenchers, such as moisture and oxygen[24–28]. Additionally, organic afterglow phosphors are typically presented in bulk forms, such as polymer films and crystals, largely limiting their applications in the fields of nanotechnology and miniaturized devices.

The use of SiO_2 as a matrix to develop afterglow microparticles (MPs) through wet chemistry methods provides a much-needed solution to the above-mentioned challenges. The abundance of hydroxyl groups in the SiO_2 matrix facilitates the stabilization of triplet states of the doped molecules through covalent and hydrogen bonding[27,29–32]. Furthermore, the rigidity of the SiO_2 matrix enables efficient separation of molecule dopants from quenchers, thereby facilitating the generation of robust afterglow, even in aqueous solutions[32–34]. In addition, conventional methods are poised to provide the groundwork for in situ molecule doping of SiO_2 matrix or the provision of uniform SiO_2 MPs for post-synthetic molecule embedding, thereby enabling the formation of afterglow phosphors[35]. Despite notable progress, achieving programmable afterglow tuning in monodisperse SiO_2 MPs with robust physiochemical stability remains a formidable challenge.

Herein, we introduce an innovative method for programmable tuning of the afterglow characteristics of monodisperse SiO_2 MPs through spatially confined emitter doping (Fig. 1a). Our methodology involves a meticulously repeated sequential doping process, where molecule emitters are precisely incorporated into different layers of monodisperse SiO_2 MPs with the formation of core@shell@shell architectures. By capitalizing on this approach, we achieve tailored afterglow emissions contingent upon the excitation wavelength by judiciously selecting molecule dopants, including 4-phenylpyridine (4-PP), 4,4′-bipyridine (4,4′-BP), and 1,8-naphthalimide (1,8-NP), each with main respective responsiveness to wavelengths at 250 nm, 290 nm, and 350 nm. This leads to the observation of distinct blue, cyan, and yellow-orange afterglows corresponding to each excitation. Furthermore, meticulous control over doping combinations enables the fabrication of 21 unique types of core@shell@shell MPs (Fig. 1b), each showcasing distinctive excitation-dependent afterglow emissions attributed to penetration-depth-dependent excitation power densities. The doping process involves a pseudomorphic transformation of the parent SiO_2 MPs in the presence of molecular dopants under hydrothermal conditions (Fig. 1c). Additionally, repeated hydrothermal treatments during the core@shell@shell MP creation facilitate the formation of progressively enhanced condensed core components (inset, Fig. 1d), leading to a gradual increase in the afterglow emission lifetime and quantum yield (QY) of the emitters in the internal layers (Fig. 1d). The uniformity of the synthesized SiO_2 MPs renders them ideal building blocks for constructing photonic crystals, enabling efficient integration of diverse optical functionalities into a unified platform conducive for multi-level information encoding and for additional possibility of afterglow regulation.

Results

Photophysical properties

We employed the synthesis of core@shell@shell SiO_2 MPs as a representative model system, wherein 4-PP, 1,8-NP, and 4,4′-BP were successively doped into the core, first shell, and second shell layers. Transmission electron microscopy (TEM) revealed the exceptional monodispersity of the resulting core@shell@shell SiO_2 MPs (Fig. 2a), boasting an average diameter of 320 nm. High-resolution TEM images further showcased the smooth surface of these resultant core@shell@shell MPs (Inset, Fig. 2a). The formation process was validated through average size examination, where reveals a gradual diameter increase from 217 nm for core MPs, advancing to 247 nm for core@shell MPs, and ultimately reaching 320 nm for the core@shell@shell MPs (Fig. 2b and Supplementary Fig. 1). Intriguingly, following each hydrothermal reaction, we noted a slight reduction in the average diameter compared to the respective parent MPs (Supplementary Fig. 2). For instance, doping 4-PP into the SiO_2 matrix via a 3 h

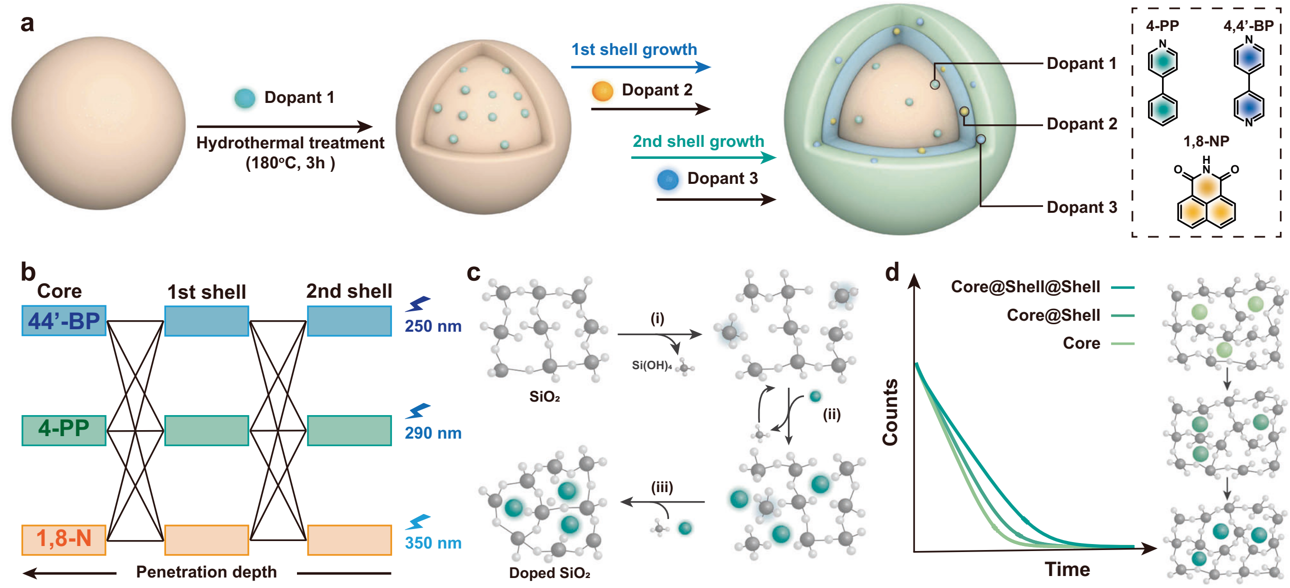

Fig. 1 | Programmable afterglow tuning in monodisperse SiO_2 MPs through spatially confined emitter doping. **a** Schematic representation of doping 4-PP, 4,4′-BP, and 1,8-NP into different layers of SiO_2 MPs. This is achieved by repeatedly performing pseudomorphic transformation of the SiO_2 matrix under hydrothermal conditions. **b** Controlled doping combinations enable the production of 21 types of excitation-dependent SiO_2 MPs. Changes in afterglow color output are due to penetration-dependent excitation power density, influenced by a combined screen effect of the outer SiO_2 matrix and the corresponding doped molecules. **c** Schematic illustration of pseudomorphic-transformation-assisted molecular doping into the SiO_2 matrix, consisting of three key steps: (i) dissolution of SiO_2, (ii) structural reconstruction, and (iii) recondensation of SiO_2. **d** Schematic illustration showing the increasing trend in the afterglow lifetime of molecular dopants within the core components as a result of repeated hydrothermal treatments, which involve doping additional molecules into the first and second shells. The inset highlights a gradual increase in the interaction between the SiO_2 matrix and the molecular dopants in the core component after each successive hydrothermal treatment.

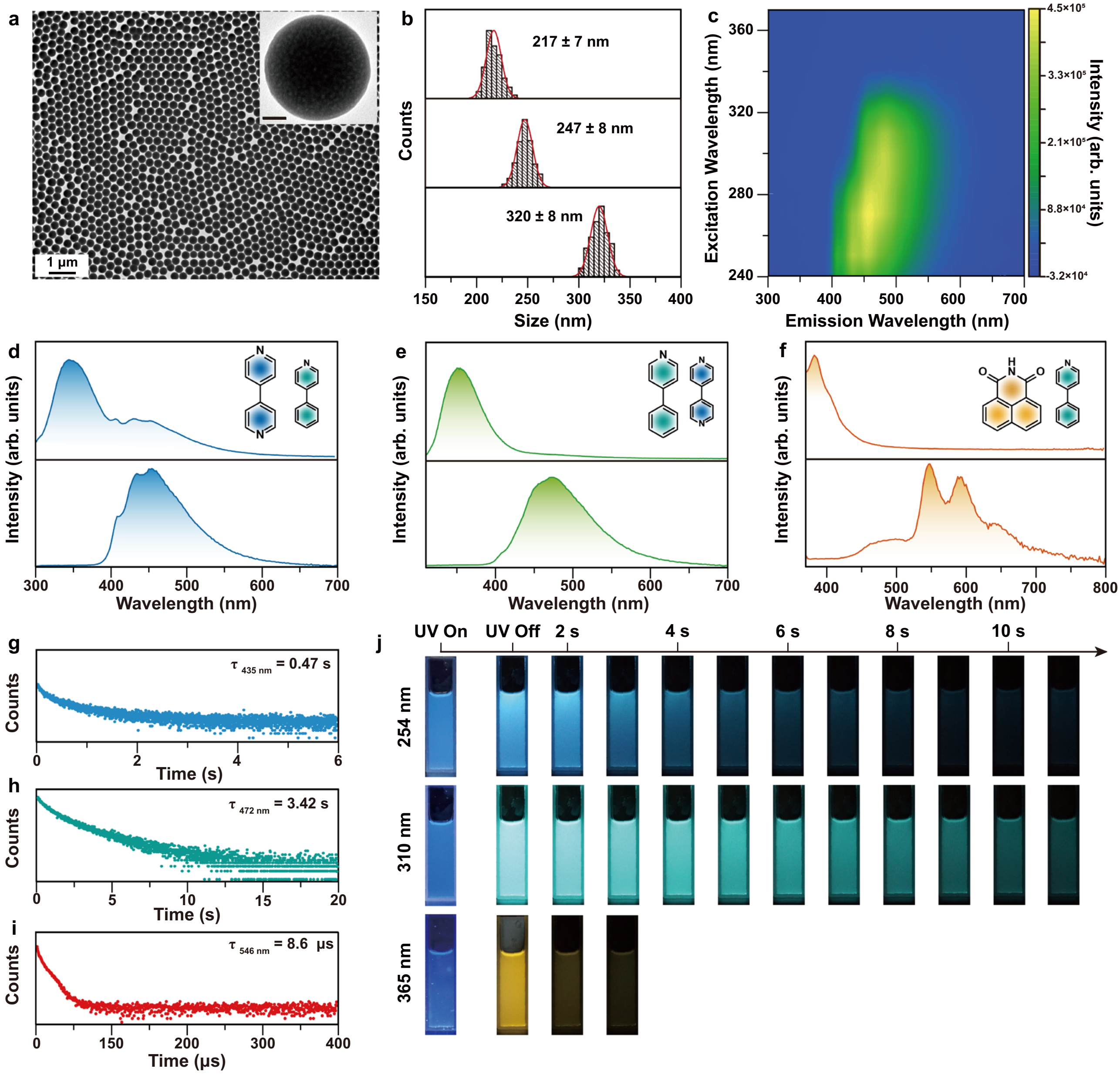

Fig. 2 | Characterization of core@shell@shell SiO_2 microparticles (MPs) doped with 4-PP, 1,8-NP, and 4,4′-BP in their core, first shell, and second shell layers, respectively. a TEM image. The inset displays a typical HRTEM image of a selected core@shell@shell SiO_2 MP. Scale bar: 50 nm. **b** Size distributions of the core, core@shell, and core@shell@shell SiO_2 MPs. Note that 200 MPs were used in the average size examination. **c** Excitation-afterglow mapping of an ethanol dispersion of the as-prepared core@shell@shell SiO_2 MPs (10 mg/mL). **d**–**f** Photoluminescence (upper panel) and afterglow emission (lower panel) of the ethanol dispersion of core@shell@shell SiO_2 MPs under excitation at 250, 290, and 350 nm. Gated time: 2 ms. Insets show the dopants under the corresponding excitations. **g**–**i** Decay curves at 435 nm for 4,4′-BP under excitation at 250 nm, 472 nm for 4-PP under excitation at 290 nm, and 546 nm for 1,8-NP under excitation at 350 nm. **j** Photographs of ethanol dispersions under excitation at 254 nm, 310 nm, and 365 nm, and after the corresponding excitations.

hydrothermal reaction at 180 °C led to a decrease from 225 nm to 217 nm in average diameter, possibly due to the partial dissolution of the parent SiO_2 matrix in the reaction mixture during the formation of 4-PP-doped SiO_2 matrix.

As expected, we observed excitation-dependent afterglow phenomena in the 4-PP-doped SiO_2@1,8-NP-doped SiO_2@4,4′-BP-doped SiO_2 MPs (Fig. 2c). To discern the origins of each emission, we synthesized corresponding singly doped SiO_2 MPs for comparison of their optical attributes. When excited at 250 nm, the core@shell@shell MPs displayed a blue color output, and the emission spectrum exhibited a prominent band at 350 nm, accompanied by tailored emissions ranging from 380 to 650 nm (Fig. 2d, upper panel). The gated spectrum indicated the persistence of the tailored emission (Fig. 2d, lower panel). When compared with the afterglow profiles of the singly doped SiO_2 MPs (Supplementary Fig. 3a), we concluded that the tailored emission comprises a mixed contribution from the dopants 4,4′-BP at 435 nm in the outermost shell and 4-PP at 472 nm in the core component. Shifting the excitation wavelength to 290 nm maintained the main emission band with minimal tail emissions in the visible spectral region (Fig. 2e, upper panel), thus sustaining the blue color output, albeit imperceptible to the naked eye due to the ultraviolet nature of the emitted light at 350 nm. Upon cessation of the excitation, a cyan afterglow emerged at 472 nm (Fig. 2e, lower panel), attributable to the long-lived emission from dopant 4-PP in the core component, accompanied with a small component of blue afterglow at 435 nm from dopants 4,4′-BP (Supplementary Fig. 3b). Further shifting the excitation wavelength to 350 nm resulted in the fluorescence band shifting to 380 nm, while afterglow emissions mainly shifted to 546 nm and 592 nm (Fig. 2f). These observations suggest the excitation of dopants 1,8-NP in the middle layer of the resultant core@shell@shell SiO_2 MPs (Supplementary Fig. 3c). Note that a shoulder afterglow was found to be located at 472 nm in this case, contributed by the dopants 4-PP in the core components. Additional controlled experiments indicated the long-lived emission of these dopants to be phosphorescence, as evidenced by the observation of a gradual increase in both afterglow intensity and lifetime with decreasing measurement temperatures (Supplementary Fig. 4). Collectively, these findings underscore the feasibility of developing excitation-dependent afterglow SiO_2 MPs through spatially confined emitter doping in their different layers.

We then investigated the lifetime of afterglow emissions produced by different dopants when stimulated with their optimal excitation wavelengths. Our findings revealed distinct lifetimes of 0.47 s, 3.42 s, and 8.6 μs for the blue afterglow of 4,4′-BP at 435 nm in the outermost shell, the cyan afterglow of 4-PP at 472 nm in the core component, and the yellow-orange afterglow of 1,8-NP at 546 nm in the first shell (Fig. 2g–i), respectively. Importantly, the lifetimes of the afterglow of the dopants doped into the core and 1st shell were notably longer compared to those observed in singly doped SiO_2 MPs of our controlled experiments (Supplementary Figs. 6d and 7d). The dense core is likely to induce the formation of a compact shell, leading to the observation of a longer afterglow lifetime for the dopants compared to the corresponding singly doped SiO_2 MPs. Upon cessation of the excitation sources, the afterglow emissions from ethanol dispersions were visibly detectable by the naked eye. Despite a slight overlap in excitation between 4-PP and 4,4′-BP, distinct blue and cyan afterglow color outputs were observed from the resultant core@shell@shell MP dispersions upon excitation at 254 and 310 nm (Fig. 2j), respectively. As expected, yellow-orange afterglow of the dispersions appears when ceasing the excitation at 365 nm.

Mechanism for RTP emission

The afterglow generation mechanism primarily arises from the stabilization of the triplet states of the doped molecules through hydrogen bonding because of the abundant presence of hydroxyl groups within the SiO_2 matrix. Additionally, the physical entrapment of the dopant molecules by the SiO_2 matrix further enhances this stabilization. Our approach offers a distinct advantage due to the pseudomorphic-transformation-assisted molecular doping strategy (Fig. 1c). The pseudomorphic transformation proceeds through three key stages: i) the surface layer of the SiO_2 MPs undergoes gradual dissolution at elevated temperatures, forming orthosilicic acid; ii) molecular dopants are introduced into the SiO_2 matrix during the dynamic equilibrium of hydrolysis and re-polymerization of the silica network; iii) upon cooling, the dissolved orthosilicic acid recondenses, further encapsulating the molecular dopants and resulting in the formation of monodisperse, afterglow molecule-doped SiO_2 MPs. In contrast, conventional Stöber method that rely on the hydrolysis of tetraethyl orthosilicate in the presence of molecule dopants failed to produce monodisperse SiO_2 MPs, despite demonstrating weak afterglow from the dopants (Supplementary Fig. 8).

Matrix rigidity plays a pivotal role in stabilizing luminescent centers. This is supported by the ^{29}Si MAS NMR spectra (Supplementary Fig. 9a), which show a significant increase in the proportion of $Si(OSi)_4$ units following hydrothermal treatment of the SiO_2 MPs—an indicator of enhanced matrix rigidity. Complementary evidence comes from Fourier transform infrared spectroscopy (FTIR), where a gradual decrease in the relative band intensity of υ(Si–OH)/δ(Si–O) was observed (Supplementary Fig. 10)[36,37], further suggesting the formation of a more rigid and confined microenvironment around the dopant molecules. To validate this mechanism, we constructed two SiO_2 structural models with different rigidity levels using GaussView 5.0 (Supplementary Fig. 9b, Supplementary Data 1). Computational analysis revealed that increasing the $Si(OSi)_4$ content not only enhances the rigidity of the matrix but also reduces the spatial separation between key atoms: specifically, the distance between hydrogen (H) atoms of 4-PP dopants and neighboring oxygen (O) atoms in the matrix decreased noticeably. Moreover, the distance between the nitrogen (N) atoms of 4-PP and hydrogen (H) atoms of the SiO_2 matrix was reduced from 3.238 Å to 1.710 Å, underscoring the stronger interactions and confinement effects induced by the more rigid matrix environment.

Mechanism for afterglow modulation

We then synthesized spatially confined triply doped core@shell@shell MPs using 5 additional combinations. Our results showed that altering the doping positions of the molecules had a marginal impact on the morphology and monodispersity of the resultant core@shell@shell MPs (Supplementary Fig. 11). However, the afterglow color output and brightness varied remarkably due to differences in the excitation power density of molecule dopants in different layers of the MPs. For example, the afterglow color output changed from golden yellow to yellow orange under 365 nm excitation when the 1,8-NP dopants were shifted from the middle layer to the outermost layer in the core@shell@shell MPs (Fig. 3a). The change in the afterglow color outputs can be further explained by the varied contribution of blue, green, orange, and red components in the emission profiles (Supplementary Fig. 12). These variations in excitation power density are attributed to the combined effects of the screen effect of the outer SiO_2 matrix and the corresponding doped molecules, as evidenced by the overlap of their UV–visible absorption spectra in the ultraviolet region (Supplementary Fig. 13). This argument is supported by the following controlled results: i) the effective absorption coefficients were estimated as 2.055×10^4 M·cm^{-1} for 4-PP at 255 nm, 9.787×10^3 M·cm^{-1} for 4,4′-BP at 239 nm, and 1.033×10^5 M·cm^{-1} for 1,8-NP at 331 nm; and ii) Upon increasing the doping concentration of 1,8-NP in the middle SiO_2 layer from 1.07×10^{-7} to 5.75×10^7 mol·g^{-1}, the afterglow intensities of 4,4′-BP in the outermost layer and 4-PP in the core component decreased exponentially and linearly, respectively (Supplementary Fig. 14).

Additionally, the core, middle layer, and outermost shell can all be doped with the same molecules to generate 3 more types of afterglow SiO_2 MPs (Supplementary Fig. 15). These findings highlight the advantage of our strategy in producing same-size MPs that carry different optical information. The excitation-afterglow mapping revealed changes in the excitation spectra after doping with 4,4′-BP, 1,8-NP, and 4-PP dopants in the core, middle layer, and outermost shell (Fig. 3b–d), indicating the successful formation of core@shell@shell MPs. The excitation-dependent afterglow emission showed significant alterations compared to counterparts doped with 4-PP, 1,8-NP, and 4,4′-BP in the core, middle layer, and outermost shell. This demonstrates the versatility of our spatially confined emitter doping strategy for creating excitation-dependent SiO_2 MPs. Further support for this approach is provided by the excitation-afterglow mapping analysis of core@shell@shell MPs with various doping combinations (Figs. 2c, 3d, and Supplementary Fig. 16).

Our strategy enables further control over the lifetime of the afterglow emission of the dopants in the resulting core@shell@shell MPs. Specifically, the lifetime of the afterglow for 4-PP doped into the core components increased from 3.26 to 3.36 and 3.42 s after the growth of the first and second shells, respectively (Fig. 3e). Similar enhancements in lifetime were observed for other dopants incorporated into the core components (Fig. 3f, g). Notably, this increase in lifetime is independent of the dopants in the outer layers, and an increase in lifetime was also observed after the growth of shells

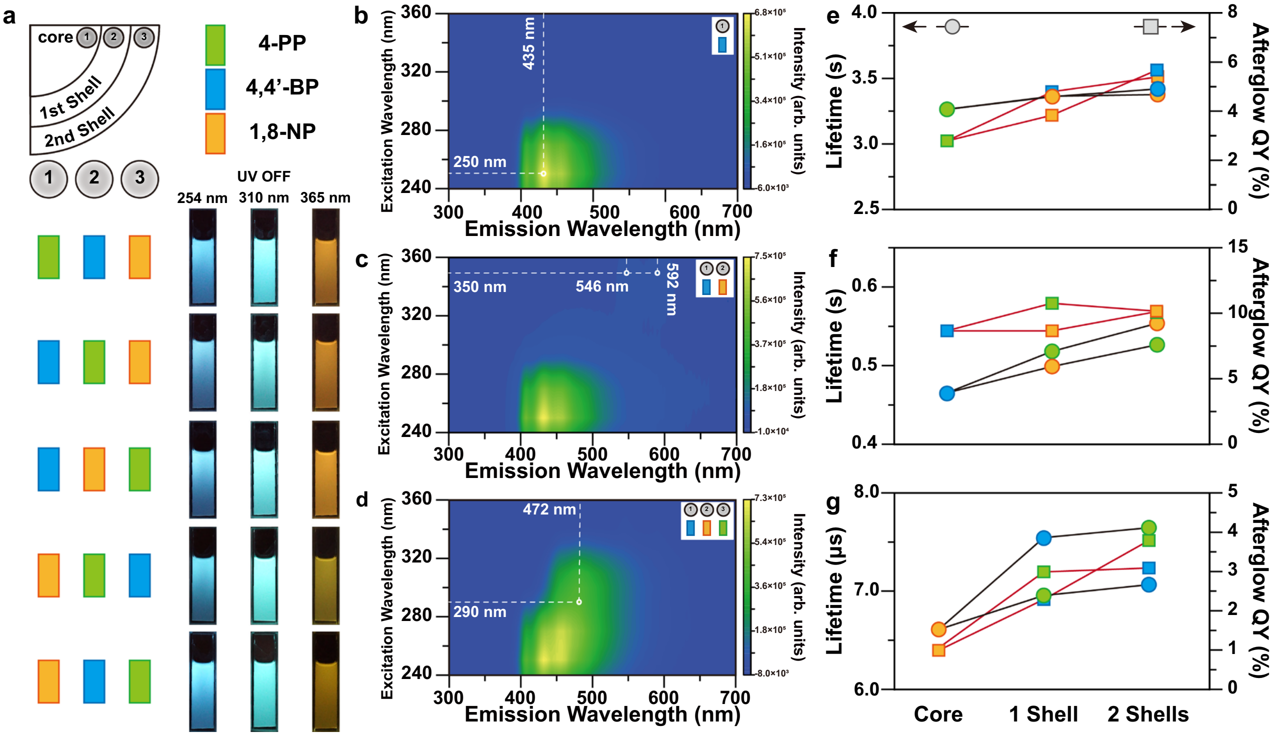

Fig. 3 | Optical characterization of triply doped core@shell@shell SiO_2 MPs. **a** Design of doping combinations with 4-PP, 4,4′-BP, and 1,8-NP dopants integrated into different layers of core@shell@shell SiO_2 MPs. Photographs of corresponding ethanol dispersions exhibit excitation-dependent afterglow. **b**–**d** Excitation-afterglow mapping for 4,4′-BP-doped SiO_2 MPs, 4,4′-BP-doped SiO_2@1,8-NP-doped SiO_2 MPs, and 4,4′-BP-doped SiO_2@1,8-NP-doped SiO_2@4-PP-doped SiO_2 MPs. Lifetime and afterglow QY measurements for (**e**) cyan afterglow after the growth of shell layers of 4,4′-BP-doped SiO_2 and 1,8-NP-doped SiO_2, (**f**) blue afterglow after the growth of shell layers of 4-PP-doped SiO_2 and 1,8-NP-doped SiO_2, and (**g**) orange afterglow after the growth of shell layers of 4-PP-doped SiO_2 and 4,4′-BP-doped SiO_2. The dependence of lifetime and afterglow QYs on the shell layer combinations is depicted by different colors of circles and squares, representing the corresponding dopants.

without molecule doping (Supplementary Fig. 17). It is worth noting that 1, 8-NP-doped SiO_2 MPs showed phosphorescence emission at about 500 nm after repeated shell growth and hydrothermal treatment, which maybe the optical characteristic of SiO_2 defects[38]. On a related note, our results showed that the growth of new SiO_2 layers—measuring 36 and 78 nm in thickness—on hydrothermally treated MPs did not result in a significant change in afterglow lifetime (Supplementary Fig. 18a–c), suggesting that the core doped components remained structurally unaffected during the layer-by-layer SiO_2 deposition. However, a gradual decrease in afterglow intensity was observed, which we attribute to UV light absorption by the outer SiO_2 shell (Supplementary Fig. 18d–f). Notably, this reduction in intensity became less pronounced as the excitation wavelength increased from 250 to 350 nm, consistent with the wavelength-dependent absorbance behavior of SiO_2 (Supplementary Fig. 18g). Additionally, spectral analysis revealed a marked improvement in the optical quality of the SiO_2 matrix, evidenced by reduced absorbance in the UV region after layer growth (Supplementary Fig. 18h), further confirming the successful formation of a more transparent and rigid outer shell. Taken together, these findings suggest that the repeated hydrothermal reactions for outer-layer molecule doping enhance interactions between the dopants and the SiO_2 matrix.

As expected, the improved interactions effectively suppress excitation loss via phonon vibration, resulting in progressively enhanced afterglow quantum yields (QYs) for the dopants (Fig. 3e–g). For example, the QYs of the afterglow for 4-PP doped into the core components increased from 2.8. to 3.9 and then to 5.7 after additional doping of 1,8-NP in the middle layer and 4,4′-BP in the outermost shell (Fig. 3e). Beyond hydrothermal treatment, the doping position combinations significantly impact the QYs of the dopants. For instance, the growth of 1,8-NP-doped SiO_2 on 4,4′-BP-doped SiO_2 layer keep the QYs of the 4,4′-BP afterglow QYs at 8.7 % (Fig. 3f). The constancy in this case is likely ascribed to the excitation overlap between 4,4′-BP and 1,8-NP, wherein the reduced afterglow QYs of the latter offsets the rise in QYs resulting from the secondary hydrothermal treatment. This fact further accounts for the observation of an increase trend in the afterglow QYs for 4,4′-BP from 8.7 to 10.8% after the growth of 4-PP and a decrease trend to 10.2% after the growth of 1,8-NP-doped SiO_2 shell.

In a subsequent set of control experiments, we investigated the effect of three distinct doping levels of molecular dopants on the afterglow properties of the resulting SiO_2 MPs (Supplementary Fig. 19). Using 4-PP-doped SiO_2@1,8-NP-doped SiO_2@4,4′-BP-doped SiO_2 MPs as a model system, we first optimized the doping concentrations of 4-PP, 1,8-NP, and 4,4′-BP. Three types of MPs were prepared by gradually increasing the concentrations of 4-PP (1.61, 4.83, and 8.05 mM), 1,8-NP (1.60, 4.80, and 8.00 mM), and 4,4′-BP (1.27, 3.80, and 6.35 mM) in the reaction mixture, respectively. The resulting doping levels were found to increase from 3.42×10^{-6} to 1.04×10^{-5} wt% for 4-PP, from 1.07×10^{-6} to 5.75×10^{-6} wt% for 1,8-NP, and from 8.60×10^{-7} to 1.21×10^{-6} wt% for 4,4′-BP. Afterglow lifetime measurements revealed negligible concentration-dependent effects for 4-PP and 4,4′-BP. In contrast, a pronounced concentration effect was observed for 1,8-NP, as indicated by a reduction in afterglow lifetime from 16.1 to 8.6 s when its doping level increased from 7.86×10^{-7} to 1.21×10^{-6} wt% (Supplementary Fig. 20).

We subsequently investigated the impact of the doping concentrations on the afterglow properties of each component within the SiO_2 MPs. Based on the previously described control experiments, the dopant concentrations were fixed at high concentration 8.05 mM for 4-PP, middle concentration 4.80 mM for 1,8-NP, and high concentration 6.35 mM for 4,4′-BP (Supplementary Fig. 21). The key findings are summarized as follows: i) Increasing the concentration of a single dopant in its corresponding SiO_2 layer, while keeping the concentrations of the other two dopants constant, led to a gradual enhancement of afterglow intensity (Supplementary Fig. 21a, d, g). This trend is attributed to the increased loading of the specific dopant in its respective layer, resulting in stronger emission. ii) Increasing the doping level of 1,8-NP in the first shell layer resulted in a gradual decrease in the afterglow intensity of the other two dopants (Supplementary Fig. 21b, f). This can be explained by the strong absorption of 1,8-NP, which reduces the excitation light available to the inner and outer layers. iii) Increasing the concentration of 4,4′-BP in the outermost layer led to a slight blue shift in the gated emission profiles (Supplementary Fig. 21c), likely due to an increased contribution of its higher-energy afterglow component. In contrast, enhancing the concentration of 4-PP in the core resulted in a red shift (Supplementary Fig. 21e), consistent with the increased presence of its lower-energy emission. iv) The afterglow properties of 1,8-NP in the first shell were largely unaffected by variations in the doping levels of 4-PP (core) and 4,4′-BP (outer shell) (Supplementary Fig. 21h, i). This is likely due to the relatively low absorbance of 4-PP and 4,4′-BP at 350 nm, combined with the higher phosphorescence quantum yield of 1,8-NP.

In addition, we investigated the effect of shell layer thickness on the optical properties of the resulting 4-PP-doped SiO_2@1,8-NP-doped SiO_2@4,4′-BP-doped SiO_2 MPs (Supplementary Fig. 22a, b, e, f). We observed that increasing the thickness of the first shell layer resulted in a gradual decrease in the afterglow intensity of 4,4′-BP (Supplementary Fig. 22c). This reduction is attributed to the strong UV absorption capability of 1,8-NP, which limits the excitation reaching the outer 4,4′-BP layer. Conversely, a slight increase in the afterglow intensity of 1,8-NP was noted with increasing first shell thickness (Supplementary Fig. 22d), likely due to more homogeneous doping throughout the thicker shell. Additionally, increasing the thickness of the outermost layer led to an enhancement in the afterglow intensity of 4,4′-BP (Supplementary Fig. 22g), which can be attributed to a higher effective doping concentration in the thicker outer shell. Importantly, this increase in outer shell thickness had no observable effect on the afterglow properties of 1,8-NP in the first shell, likely due to the distinct excitation profiles of the two dopants (Supplementary Fig. 22h).

Additionally, we found that although the one-pot hydrothermal reaction can produce triply doped SiO_2 MPs with high monodispersity, the excitation-dependent afterglow performance retained (Supplementary Fig. 23a). However, the under excitation at 310 nm, the blue afterglow of 4-PP dopants become distinguished and the remarkably affect the cyan afterglow for 4-PP dopants (Supplementary Fig. 23e). This is likely because 4,4′-BP dopants exhibit afterglow with a high QYs of 8.7%, 3.1-fold stronger than that of 4-PP. Furthermore, the one-pot hydrothermal reaction resulted in afterglow emissions with shorter lifetimes. For instance, the afterglow lifetime of 4-PP dopants in the MPs was estimated to be 3.2 s, lower compared to that observed in the core@shell@shell MPs (Supplementary Fig. 23c). This is due to weaker interactions between the dopants and the SiO_2 matrix in the MPs produced by the one-pot hydrothermal reaction. In addition, the doping levels were estimated to be 4.48×10^{-7} mmol g^{-1} for 4-PP, 1.74×10^{-6} mmol g^{-1} for 4,4′-BP, and 2.74×10^{-7} mmol g^{-1} for 1,8-NP in SiO_2 matrix when fixing the dopant concentrations at the same level (8×10^{-6} mM) in the precursor solution (Supplementary Fig. 24). The different doping capability of these molecule emitters in SiO_2 matrix further highlights the benefits of spatially confined emitter doping over one-pot doping in control of the afterglow properties of SiO_2 MPs.

As an added benefit, our strategy enables the preparation of excitation-dependent afterglow SiO_2 MPs with spatially confined binary doping. This design allows for the creation of 6 additional types of afterglow SiO_2 MPs. These MPs exhibited similar excitation-afterglow attributes under optimized excitation conditions (Supplementary Fig. 25). Notably, without 4-PP doping, the resultant core@shell SiO_2 MPs produced a deep blue afterglow from 4,4′-BP under excitation at 254 nm and a bright orange afterglow from 1,8-NP dopants under excitation at 365 nm (Supplementary Fig. 26). As expected, due to the medium interaction strength between the dopants and the SiO_2 matrix, the afterglow lifetime of these dopants in the core components was significantly longer than that of singly doped SiO_2 MPs but shorter than that of triply doped SiO_2 MPs.

Additionally, the structural information of afterglow MPs can be retrieved from a reference library. We begin by systematically collecting the afterglow properties of various molecule-doped SiO_2 MPs, including their lifetimes and quantum yields under different excitation wavelengths (250, 290, and 350 nm). These data are compiled into a searchable database using MATLAB. Given that spatially confined dopant molecules exhibit distinct characteristics due to differences in excitation density and matrix rigidity, the afterglow behavior of an unknown doped SiO_2 MP can be used to infer its structural configuration. By inputting key parameters—such as afterglow lifetimes and quantum yields—into the database, the most probable structural match can be identified. For example, inputting the parameters shown in Supplementary Fig. 27a quantum yield of 10.2% under 250 nm excitation and a lifetime of 3.28 s under 290 nm excitation—returns a match of "B–P–N", corresponding to 4,4′-BP (B)-doped SiO_2@4-PP (P)-doped SiO_2@1,8-NP (N)-doped SiO_2 (Supplementary Software).

Applications

Our strategy of doping molecular emitters into SiO_2 MPs enables the preparation of uniform, multicolored afterglow building blocks for advanced photonic crystals. These photonic crystal structures can encode multi-dimensional information within their patterns by displaying distinct color output variations under different irradiation conditions (Fig. 4a). As a proof-of-concept experiment, we prepared a photonic crystal structure using a dip-coating strategy with 4-PP-doped SiO_2@1,8-NP-doped SiO_2@4,4′-BP-doped SiO_2 MPs as building blocks. This structure was further patterned into a flower shape using a laser beam. Highly ordered superstructures were observed via scanning electron microscopy (SEM), revealing the formation of a close-packed hexagonal pattern with a thickness of 3.38 m and a periodicity of 340.1 nm (Fig. 4 b and Supplementary Fig. 28). As expected, the flower-shaped photonic crystals exhibited angle-dependent reflectance spectra, with a gradual blueshift in the reflectance band from 639 to 488 nm as the incident angle increased from 10° to 60° (Fig. 4c). With an increase in the average diameter from 217 nm for core MPs to 247 nm for core@shell MPs and 320 nm for core@shell@shell MPs, the photonic crystal structures showed size-dependent color outputs as a function of the incident angle (Fig. 4d, and Supplementary Fig. 29). At an incident angle of 10°, the flower-shaped photonic crystal structures comprising core, core@shell, and core@shell@shell SiO_2 MPs displayed color outputs of blue, yellow, and red, respectively (Figs. 4e and 4f). Notably, the photonic crystal structure comprising core@shell@shell MPs allowed the patterned flower to undergo a structural color transition from red to green to violet, covering the entire visible spectrum as the incident angle increased from 10° to 70°. These observations can be explained by the following equation[39,40].

$$\lambda_{\max} = 1.633(d/m)(n_a^2\text{-}\sin^2\theta)^{1/2}$$

where d represents the diameter of the MPs, m and θ represent the Bragg reflection order and the angle between the normal and incident light, respectively. The value of n_a is defined as the weighted sum of the refractive indices of the MP portion and the gap portion. The change in both the angle between the normal and incident light and the diameter of the SiO_2 MPs lead to the corresponding change in the wavelength of the photons scattered.

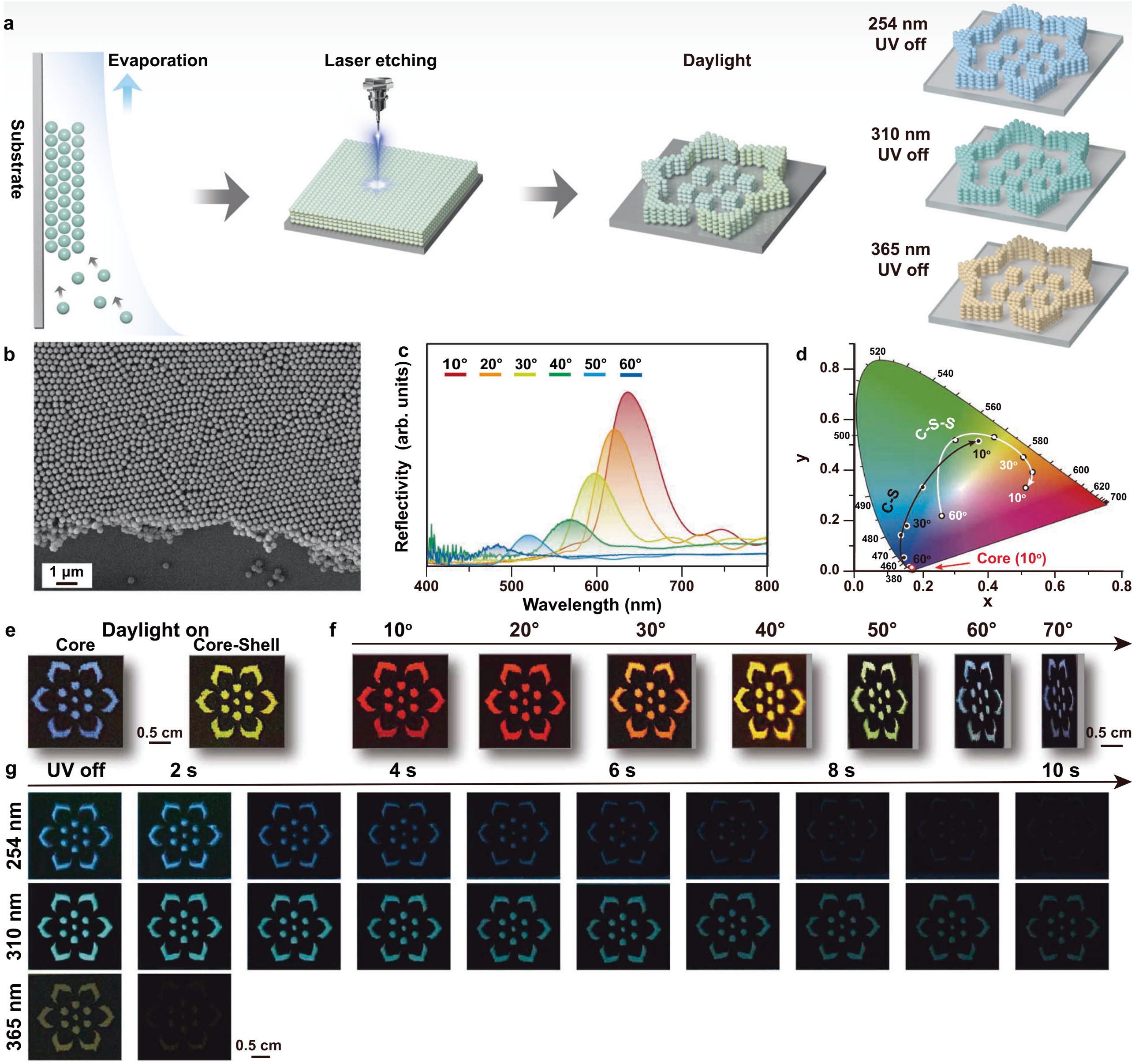

Fig. 4 | Application of excitation-dependent afterglow core@shell@shell SiO_2 MPs in photonic crystal fabrication. **a** Schematic illustration of the fabrication process for flower-shaped photonic crystals. This process begins with a sequential dip-coating method, followed by laser-assisted etching to precisely sculpt the photonic crystal patterns into flower shapes. The synthesis utilizes 4-PP-doped SiO_2@1,8-NP-doped SiO_2@4,4′-BP-doped SiO_2 MPs as building blocks. **b** SEM image of the as-prepared photonic crystal. **c** Reflectance spectra of the photonic crystal at different incident angles. **d** Trajectory of structural color modulation for photonic crystals in the CIE coordinate diagram. The photonic crystals were created using 4-PP-doped SiO_2 MPs (red point), 4-PP-doped SiO_2@1,8-NP-doped SiO_2 (black point), and 4-PP-doped SiO_2@1,8-NP-doped SiO_2@4,4′-BP-doped SiO_2 MPs (white point) as building blocks, respectively. **e** Structural color outputs of the fabricated flower-shaped photonic crystals composed of 4-PP-doped SiO_2 MPs and 4-PP-doped SiO_2@1,8-NP-doped SiO_2 MPs under natural daylight at an observation angle of 10°. **f** Angle-dependent structural color outputs of the fabricated flower-shaped photonic crystals comprising the core@shell@shell SiO_2 MPs as building blocks under natural daylight. **g** Time-dependent afterglow images of the flower-shaped photonic crystals under excitation wavelengths of 254, 310, and 365 nm.

Notably, upon irradiation at distinct wavelengths—specifically 254, 310, and 365 nm—diverse afterglow scenarios were generated due to the primary excitation shifting among the dopants. With excitation fixed at 254 nm, the predominant excitation of 4,4′-BP embedded in the second shell resulted in a blue afterglow with an extended persistence of about 6 s. Shifting the excitation wavelength to 310 nm led to the predominant excitation of 4-PP dopants in the core, producing a cyan afterglow that lasted up to 10 s. Additionally, excitation at 365 nm, targeting 1,8-NP dopants, gave rise to a yellow afterglow with a brief duration of less than 2 s. These findings highlight the adaptability of afterglow color and lifetimes in core@shell@shell SiO_2 MPs through spatially confined emitter doping. This adaptability enables the creation of a versatile library of optical MPs, suitable for developing advanced photonic crystal platforms for complex optical information encoding. On a separate note, by customizing the spatial arrangement of the 15 particle types as shown in Fig. 3g, the system achieves a total storage capacity of 45 trits, equivalent to approximately 71.3 bits (Supplementary Fig. 30)[41].

In addition, we demonstrated that the as-prepared 4-PP-doped SiO_2@1,8-NP-doped SiO_2@4,4′-BP-doped SiO_2 MPs are well-suited for applications in multispectral delayed display when integrated with customized printed circuit board (Supplementary Fig. 31). An integrated circuit board was fabricated incorporating three LEDs with distinct emission wavelengths (250 nm, 290 nm, and 350 nm), programmed to emit synchronized 1-s pulses in sequence. Upon sequential activation, persistent afterglow emissions were observed following the cessation of both 290 nm and 350 nm excitations. This unique property enables multispectral delayed display even after the excitation sources are turned off. Remarkably, when 350 nm pulses were applied at 1-s intervals after the 290 nm excitation had ceased, a time-dependent evolution of the afterglow signal was recorded under monochromatic stimulation, highlighting the potential of these afterglow SiO_2 MPs for multispectral delayed display.

Discussion

Compared with previously reported systems for afterglow tuning, our approach demonstrates several key advantages. First, it enables precise modulation of both emission wavelength and lifetime by controlling dopant concentrations layer by layer within SiO_2 MPs. This spatially selective doping strategy facilitates the rational design of MPs with tailored optical properties—something difficult to achieve through traditional simultaneous multi-dopant methods. Second, whereas molecule-doped polymers and crystals typically exhibit afterglow only in the solid state due to poor solvent resistance, our SiO_2 matrix maintains its afterglow performance across a wide range of organic solvents (Supplementary Fig. 32), including cyclohexane, petroleum ether, ethyl acetate, and dichloromethane. Third, our molecule-doped afterglow SiO_2 MPs exhibited superior afterglow stability compared to commercial phosphors. In contrast, the afterglow of $SrAl_2O_4$:Eu,Dy phosphors was completely quenched after 12 h of storage in aqueous solution due to hydrolysis and structural degradation (Supplementary Fig. 33). Fourth, this robust doping platform supports the reliable construction of an extended library of afterglow MPs with customizable photophysical features (Supplementary Fig. 34). Our results demonstrated that: (i) the afterglow emission bands exhibited broad tunability from 416 to 578 nm depending on the choice of molecular dopants; (ii) 4-PP showed the longest afterglow lifetime of 3.25 s, with an afterglow quantum yield of 2.8%; and (iii) 9-phenylacridine achieved the highest afterglow quantum yield of 22.9%, albeit with a shorter lifetime of 2 ms (Supplementary Fig. 35).

Moreover, the synthesis process offers excellent scalability, cost-effectiveness and environmental friendliness. We have successfully scaled the reaction up to 12.18 g per batch, with the only limitation being reactor volume (Supplementary Fig. 36). The high reactivity of the freshly formed SiO_2 matrix facilitates further scale-up by simply enlarging the reactor. The entire process is economically advantageous: the tetraethyl orthosilicate (TEOS) precursor is inexpensive, undoped dopants can be recovered and reused, and water is employed as the reaction solvent. These features not only bring the production cost down to approximately $0.20 USD per gram—substantially lower than that of most polymer- and crystal-based systems, but also offer a sustainable alternative to conventional synthesis approaches.

Finally, our strategy allows for the fabrication of monodisperse afterglow SiO_2 MPs, which greatly simplifies the assembly of photonic crystal structures. These ordered assemblies not only support multiple optical functionalities for information encoding but also introduce photonic stopbands, enabling further tuning of solid-state afterglow behavior through photonic–emissive coupling. Beyond optical applications, the resulting MPs exhibit excellent stability and biocompatibility (Supplementary Fig. 37), highlighting their potential for use in biosensing and biomedical imaging.

Methods

Preparation of monodisperse SiO_2 MPs

Monodisperse SiO_2 colloidal MPs were prepared by a modified Stöber method. In a typical experiment, 33 mL of DI water, 160 mL of ethanol, and 3.5 mL of ammonia solution (25%-28%) were first mixed and heated to 60 °C. Next, 4.4 mL of TEOS was added dropwise to this solution, and the reaction was continued for 30 min under stirring to form the seed solution. A certain volume of the seed solution was then mixed with 10 mL of TEOS to form a clear mixture. Aqueous ammonia was added to the resultant mixture, and the mixture was allowed to react at room temperature for 10 h. The average diameter of the resulting SiO_2 colloidal MPs was estimated to be 225 nm when 4 mL of the volume of the seed solution was use. After the reaction, the product was centrifuged and washed several times with ethanol.

Preparation of afterglow molecule-doped SiO_2 MPs

In brief, a mixture of molecule (5 mg) and SiO_2 MPs (50 mg, 4 mL water) was prepared which mixed at 5 mL glass baker. The baker was transferred to a 20-mL polytetrafluoroethylene hydrothermal reactor and heated at 180 °C for 3 h. After cooling to room temperature, the resulting mixture was centrifuged at 10,142 x g for 5 min. The precipitate was purified through 3 cycles of alternate centrifugation and dispersion with ethanol, and the final precipitate was dispersed in 3 mL of ethanol solution.

Fabrication of photonic crystal structures

The substrates for building the photonic structures were washed with ethanol before use. The dip-coating process was carried out at room temperature using a dip-coater, and the pulling rate was set at 2 $\mu m\ s^{-1}$.

Characterization

Transmission electron microscopy was carried out on a HT7800 operating at an acceleration voltage of 100 kV. Scanning electron microscopy was performed using a Gemini SEM 300 (ZEISS). Photoluminescence emission profiles and decay curves were obtained using an FLS-1000 instrument from Edinburgh Instruments Ltd. Photoluminescence quantum yield (PLQY) measurements were performed with a C9920-02G instrument from Hamamatsu. The low-temperature spectroscopy tests are conducted using the Oxford OptistatDN liquid nitrogen cryostat. UV-vis absorption spectra were taken on a Hitachi U-3900H ultraviolet-visible spectrophotometer. Dynamic Light Scattering profiles were measured by Malvern Zeta sizer nano ZS. ^{29}Si solid-stateNMR was performed by a nuclear magnetic resonance spectrometer with a super-conducting magnet (Bruker, Avance III HD 400 MHz). The photonic crystals were prepared using a dip-coating instrument (SYDC-100H, SAN-YAN Instrument Co. Ltd., Shanghai). The angle-dependent reflection spectra of the prepared photonic crystals were measured using an angular resolution spectral system (R1, Shanghai Fuxiang Optical Co. Ltd., Shanghai). A standard Al mirror (Ideaoptics STD-M) was used to serve as the ideal reflector reference.

Computational details

Based on the theoretical correlation between decreasing y and z values and enhanced matrix rigidity in the Si39OyHz system, two distinct Si-O matrix models (low rigidity: $y = 111$, $z = 66$; high rigidity: $y = 102$, $z = 48$) was constructed using GaussView 6.0, followed by embedding a 4-PP molecule. All structures were fully optimized at the B3LYP/6-31 + G(d) level of theory in Gaussian 09.

Data availability

The data that support the findings of this study have been included in the main text and supplementary information. All other information can be obtained from the corresponding author upon request. Source data are provided with this paper.

References

1. Chen, Q. et al. Long lifetimes white afterglow in slightly crosslinked polymer systems. *Nat. Commun.* **15**, 2947 (2024).

2. Jiang, K. et al. Enabling robust and hour-level organic long persistent luminescence from carbon dots by covalent fixation. *Light Sci. Appl.* **11**, 80 (2022).
3. Chen, K. et al. Twofold rigidity activates ultralong organic high-temperature phosphorescence. *Nat. Commun.* **15**, 1269 (2024).
4. Li, G. et al. High-performance ultraviolet organic light-emitting diodes enabled by double boron–oxygen-embedded benzo[*m*] tetraphene emitters. *J. Am. Chem. Soc.* **146**, 1667–1680 (2024).
5. Wang, H. et al. Abnormal thermally-stimulated dynamic organic phosphorescence. *Nat. Commun.* **15**, 2134 (2024).
6. Xiong, S. et al. Achieving tunable organic afterglow and UV-irradiation-responsive ultralong room-temperature phosphorescence from pyridine-substituted triphenylamine derivatives. *Adv. Mater.* **35**, 2301874 (2023).
7. Peng, F. et al. Tunable, excitation-dependent, and water stimulus-responsive room-temperature phosphorescence cellulose for versatile applications. *Adv. Mater.* **35**, 2304032 (2023).
8. Li, D. et al. Completely aqueous processable stimulus responsive organic room temperature phosphorescence materials with tunable afterglow color. *Nat. Commun.* **13**, 347 (2022).
9. Lu, G. et al. Delayed room temperature phosphorescence enabled by phosphines. *Nat. Commun.* **15**, 3705 (2024).
10. Li, L. et al. Finely manipulating room temperature phosphorescence by dynamic lanthanide coordination toward multi-level information security. *Nat. Commun.* **15**, 3846 (2024).
11. Guo, D. et al. Visible-light-excited robust room-temperature phosphorescence of dimeric single-component luminophores in the amorphous state. *Nat. Commun.* **15**, 3598 (2024).
12. Chang, B., Chen, J., Bao, J., Su, T. & Cheng, Z. Molecularly engineered room-temperature phosphorescence for biomedical application: from the visible toward second near-infrared window. *Chem. Rev.* **123**, 13966–14037 (2023).
13. Liang, Y. et al. UV-curing-enhanced organic long-persistent luminescence materials. *Adv. Mater.* **35**, 2304820 (2023).
14. Zheng, K., Zhang, Y., Li, B. & Granick, S. Phosphorescent extensophores expose elastic nonuniformity in polymer networks. *Nat. Commun.* **14**, 537 (2023).
15. Chen, J., Lu, Y. & Chen, J. Generation of long-lived excitons in room-temperature phosphorescence 2D organic and inorganic hybrid perovskites for ultrafast and low power-consumption nonvolatile photomemory. *Adv. Sci.* **10**, 2301028 (2023).
16. Yu, X. et al. Time-dependent polychrome stereoscopic luminescence triggered by resonance energy transfer between ccarbon dots-in-zeolite composites and fluorescence quantum dots. *Adv. Mater.* **35**, 2208735 (2023).
17. Zhou, B., Qi, Z. & Yan, D. Highly Efficient and Direct Ultralong All-phosphorescence from metal-organic framework photonic glasses. *Angew. Chem. Int. Ed.* **61**, e202208735 (2022).
18. Zhang, K. et al. Aromatic Amides: A Smart Backbone toward isolated ultralong bright blue-phosphorescence in confined polymeric films. *Angew. Chem. Int. Ed.* **62**, e202300927 (2023).
19. Zhang, X. et al. Ultralong phosphorescence cellulose with excellent anti-bacterial, water-resistant and ease-to-process performance. *Nat. Commun.* **13**, 1117 (2022).
20. Hamzehpoor, E. et al. Efficient room-temperature phosphorescence of covalent organic frameworks through covalent halogen doping. *Nat. Chem.* **15**, 83–90 (2023).
21. Zhao, W., He, Z. & Tang, B. Room-temperature phosphorescence from organic aggregates. *Nat. Rev. Mater.* **5**, 869–885 (2020).
22. Wan, K. et al. Structural materials with afterglow room temperature phosphorescence activated by lignin oxidation. *Nat. Commun.* **13**, 5508 (2022).
23. Zeng, M. et al. Enabling robust blue circularly polarized organic afterglow through self-confining isolated chiral chromophore. *Nat. Commun.* **15**, 3053 (2024).
24. Wang, X., Zhao, B. & Deng, J. Liquid crystals doped with chiral fluorescent polymer: multi-color circularly polarized fluorescence and room-temperature phosphorescence with high dissymmetry factor and anti-counterfeiting application. *Adv. Mater.* **35**, 2304405 (2023).
25. Lou, Q. et al. Thermally enhanced and long lifetime red TADF carbon dots via multi-confinement and phosphorescence assisted energy transfer. *Adv. Mater.* **35**, 2211858 (2023).
26. Yang, X., Waterhouse, G. I. N., Lu, S. & Yu, J. Recent advances in the design of afterglow materials: mechanisms, structural regulation strategies and applications. *Chem. Soc. Rev.* **52**, 8005–8058 (2023).
27. Huang, Q. et al. Ultrastable and colorful afterglow from organic luminophores in amorphous nanocomposites: advanced anti-counterfeiting and in vivo imaging application. *Nano Res* **13**, 1035–1043 (2020).
28. Zhang, Y. et al. Ultraviolet irradiation-responsive dynamic ultralong organic phosphorescence in polymeric systems. *Nat. Commun.* **12**, 2297 (2021).
29. Liang, Y. et al. Ultralong and efficient phosphorescence from silica confined carbon nanodots in aqueous solution. *Nano Today* **34**, 100900 (2020).
30. Zhang, D. et al. On-demand circularly polarized room-temperature phosphorescence in chiral nematic nanoporous silica films. *Adv. Optical Mater.* **10**, 2102015 (2022).
31. He, J. et al. Anchoring carbon nanodots onto nanosilica for phosphorescence enhancement and delayed fluorescence nascence in solid and liquid states. *Small* **16**, 2005228 (2020).
32. He, T. et al. Ratiometric hypoxia detection by bright organic room temperature phosphorescence of uniformed silica nanoparticles in water. *Aggregate* **4**, e250 (2023).
33. Chen, J. et al. Dynamic room temperature phosphorescence of silane-functionalized carbon dots confining within silica for anti-counterfeiting applications. *Small* **20**, 2306323 (2024).
34. Sun, Y. et al. Ultralong lifetime and efficient room temperature phosphorescent carbon dots through multi-confinement structure design. *Nat. Commun.* **11**, 5591 (2020).
35. Chen, X. et al. Pseudomorphic synthesis of monodisperse afterglow carbon dot-doped SiO_2 microparticles for photonic crystals. *Adv. Mater.* **35**, 2307198 (2023).
36. Mishra, A. K., Narayan, R., Aminabhavi, T. M., Pradhan, S. K. & Raju, K. V. S. N. Hyperbranched polyurethane (HBPU)–urea and HBPU–imide coatings: effect of chain extender and NCO/OH ratio on their properties, *Prog. Org. Coat.* **74**, 134–141 (2012).
37. Kačuráková, M. & Wilson, R. H. Developments in mid-infrared FT-IR spectroscopy of selected carbohydrates. *Carbohydr. Polym.* **44**, 291–303 (2001).
38. Chen, X. et al. Matrix-induced defects and molecular doping in the afterglow of SiO_2 microparticles. *Nat. Commun.* **15**, 8111 (2024).
39. Ge, J. & Yin, Y. Responsive photonic crystals. *Angew. Chem. Int. Ed.* **50**, 1492–1522 (2011).
40. Cai, Z. et al. From colloidal particles to photonic crystals:advances in self-assembly and their emerging applications. *Chem. Soc. Rev.* **50**, 5898–5951 (2021).
41. Georgescu, I. A bit on the bit. *Nat. Phys.* **12**, 888 (2016).

Acknowledgements

This work is supported by the National Natural Science Foundation of China (grant numbers 22075228 and 62475218), and the Joint Research Funds of the Department of Science & Technology of Shaanxi Province and Northwestern Polytechnical University (No. 2020GXLH-Z011), the Fundamental Research Funds for the Central Universities (grant numbers 0515022GH0202036 and 0515022SH0201036), and the Natural Science Foundation of Shaanxi (2024JC-YBQN-0104).

Author contributions

X.L. and W.H. conceived and supervised the project. X.C., C.P. and Z.G. designed the experiments. X.C. carried out the afterglow microspheres synthesis and optical measurements. T.B. and Z.G. captured the afterglow images. Z.W. and W.X provided insightful discussion. X.C and X.L. wrote the manuscript with input from other authors.

Competing interests

The authors declare no competing interests.

Additional information

Supplementary information The online version contains supplementary material available at https://doi.org/10.1038/s41467-025-63901-5.

Correspondence and requests for materials should be addressed to Xiaowang Liu or Wei Huang.

Peer review information *Nature Communications* thanks the anonymous reviewers for their contribution to the peer review of this work. A peer review file is available.

Reprints and permissions information is available at http://www.nature.com/reprints